Vertical Orbit Excursion FFAGs

Stephen Brooks[*]
RAL, Chilton, OX11 0QX, UK
(Dated: April 30, 2013)

FFAGs with vertical orbit excursion (VFFAGs) provide a promising alternative design for rings with fixed-field superconducting magnets. They have a vertical magnetic field component that increases with height in the vertical aperture, yielding a skew quadrupole focussing structure. Scaling type VFFAGs are found with fixed tunes and no intrinsic limitation on momentum range. This paper presents the first multi-particle tracking of such machines. Proton driver rings to accelerate the 800 MeV beam from the ISIS synchrotron are presented, in terms of both magnet field geometry and longitudinal behaviour during acceleration with space charge. The 12 GeV ring produces an output power of at least 2.18 MW. Possible applications of VFFAGs to waste transmutation, hadron therapy and energy-recovery electron accelerators are also discussed.

I. VFFAG PRINCIPLE

If the closed orbit of a ring accelerator lies in a horizontal plane (constant y), the magnetic field along it must satisfy $\oint B_y \, ds = 2\pi p/q$ in order for the orbit to close. This can be satisfied by many magnetic fields, some of which permit vertical orbit excursion. If B_y increases with y, the closed orbit will move in the $+y$ direction (upwards) as p increases, so that $\oint B_y \, ds$ remains proportional to beam momentum.

It is a misconception to think that 'centrifugal force' always moves the orbit outwards as momentum increases in a fixed field machine. In fact the beam adiabatically tracks the closed orbit provided that it has locally stable optics. In the vertical excursion case, any initial outward movement from centrifugal force moves particles horizontally into regions where the vertical field gradient implies (via $\nabla \cdot \mathbf{B} = 0$) that there is a B_x component, which then pushes the particles upwards as required.

Fig. 1 shows an example of the motion of a beam in such an accelerator with increasing energy, where relativistic shrinkage of the beam is also visible.

A. Linear Optics of Scaling VFFAGs

This paper concentrates on what could be termed the *scaling* vertical-orbit-excursion field by analogy with (horizontal) scaling FFAGs. The magnetic fields in scaling machines are derived from a symmetry principle. If a closed orbit is scaled by a factor a in size (and possibly translated or rotated) while magnetic fields on that orbit are scaled by b, then the beam momentum $p \propto B\ell$ must scale by ab. Scaling FFAGs use a group of transformations that scale about the ring centre with $b = a^k$ [1] for some *field index* k. Scaling VFFAGs as defined here use a group of translations for which $a = 1$ but $b = e^{k\Delta y}$ for vertical orbit offset Δy. k must be constant for the entire
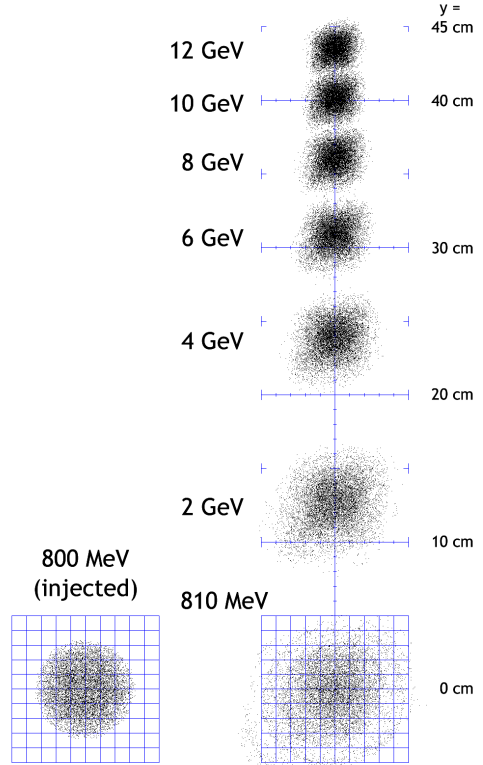
———————
[*] stephen.brooks@stfc.ac.uk

FIG. 1. Vertical movement of a proton beam accelerated in a scaling VFFAG with $k = 5\,\mathrm{m}^{-1}$ [2].

ring to satisfy the scaling law

$$y \mapsto y + \Delta y, \qquad (p, \mathbf{B}) \mapsto (p, \mathbf{B})e^{k\Delta y},$$

which ensures the geometry of all particle trajectories, including those off the closed orbit, are preserved during acceleration: translating upwards as p is increased.

Thus, the field within the body of a scaling VFFAG magnet is given by $B_y = B_0 e^{ky}$ on the $x = 0$ mid-plane. The beam travels in the local $+z$ direction through each magnet and shifts to height $y = \frac{1}{k} \ln p/p_{\mathrm{inj}}$ as momentum p increases. The injection orbit is defined to be at

$y = 0$ and the current windings lie on the $\pm x$ sides of a vertical gap (see Figs. 3 and 5). At injection, the magnet body has bending field B_0 and skew gradient $B_0 k$ (as well as higher multipoles of strength proportional to $B_0 k^{n \geq 2}$), so without edge effects B_0 must alternate in sign to provide alternating gradient focussing. Optics of a ring with such magnets without edge effects are considered in [2], including scans of the lattice stability regions to find which have good dynamic aperture in spite of the nonlinear fields.
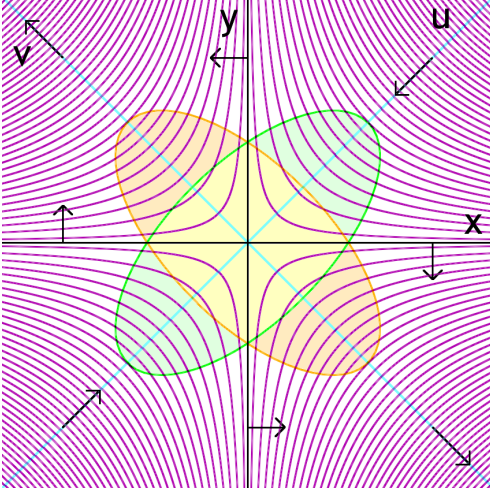

FIG. 2. Skew quadrupole magnetic field (purple lines) and direction of forces (arrows) exerted on the beam, which in a skew FODO channel oscillates in shape between the two ellipses shown. The new skew axes u, v are labelled.

As in scaling FFAGs, this magnetic field is combined function, with a dipole and gradient (and all higher multipoles) superimposed. For small distances from the origin, the field is to first order

$$B_y = B_0 + B_0 k y + \cdots$$
$$B_x = \quad - B_0 k x + \cdots ,$$

which produces skew focussing optics as shown in Fig. 2. Is it useful to define skew transverse axes

$$u = (x + y)/\sqrt{2} \qquad v = (y - x)/\sqrt{2},$$

which are rotated by $45°$. Using these, the usual expression for a quadrupole field reappears:

$$B_u = (B_x + B_y)/\sqrt{2} = B_0/\sqrt{2} + B_0 k (y - x)/\sqrt{2}$$
$$= B_0/\sqrt{2} + B_0 k v$$
$$B_v = (B_y - B_x)/\sqrt{2} = B_0/\sqrt{2} + B_0 k (x + y)/\sqrt{2}$$
$$= B_0/\sqrt{2} + B_0 k u.$$

Another important feature shared with scaling FFAGs is that optics are identical at each momentum, so tunes stay constant, which is important for proton machines with many turns or significant space charge.

B. Combination with Existing FFAG Types

For most horizontal orbit excursion FFAGs, there is a VFFAG with the same focussing structure, similar orbit separation and field gradients, except the separation becomes vertical and the gradients skew. The VFFAG may also be combined with fixed or variable frequency RF acceleration schemes.

In scaling VFFAGs, field gradient is proportional to the bending field, which has the unfortunate consequence of requiring reverse bends in all alternating gradient lattices. Having negative B_0 for some magnets in this way increases machine circumference for a given field by ~ 5 times, similar to the circumference factor [3] in horizontal scaling FFAGs. The parameter space for scaling FODO and triplet VFFAG lattices is plotted in [2], showing most of the stable region stays close to the F=D line where net bending is zero. This can be mitigated somewhat by using edge angles on the magnets for the alternating focussing and the interior field for bending, permitting a single magnet per lattice cell. This technique is the equivalent of the 'spiral sector' scaling FFAG and is used in the proton driver machine presented in sections III and IV; it is also commonly used in cyclotrons.

Non-scaling VFFAGs are also possible but as with horizontal non-scaling FFAGs, tunes may no longer be fixed and momentum range may be limited. Additionally, the closed orbits will not necessarily stack vertically on top of each other due to the different horizontal bending experienced by different momenta in each magnet, meaning the orbit excursion could sweep out a generalised curved surface. Linear-field non-scaling VFFAGs, suggested by [4], can be constructed using only offset skew quadrupoles, though their beam dynamics is at present completely unexplored.

Adding a synchrotron-like RF system to a VFFAG permits acceleration of bunches of any energy, with the RF frequency tracking the ring revolution frequency, provided the RF has the appropriate aperture slot for the beam orbit excursion. Fixed-frequency RF can also be considered for relativistic beams, since the VFFAG closed orbit circumference does not change very much with energy and is constant in scaling VFFAGs, making the ring nearly isochronous as $v \to c$. This could enable cyclotron-like CW operation for some machines.

C. Historical Papers

The earliest mention of the VFFAG principle the author is aware of is Ohkawa [5] in 1955, who suggested a scaling VFFAG for electrons with fixed-frequency RF, calling it an FFAG cyclotron with fixed orbit length. Leleux et al. [6] in 1959 again found the exponential field configuration and analysed its linear dynamics and stability in their report. They call it a 'helicoidal FFAG' after the helical progression of the orbit upwards in the ring as it is accelerated. Teichmann [7] in 1962 had continued

developing Ohkawa's idea in order to achieve 'complete isochronism', that is a fixed-tune isochronous FFAG and presents an interesting figure showing that a deviation from exact vertical orbit excursion can make the orbits of even sub-relativistic particles exactly isochronous. This will be revisited briefly in section V B.

The author developed most of these ideas independently starting in 2009, discovering this literature later with the help of colleagues. New developments in the intervening half century include the widespread use of computerised multi-particle tracking and superconducting magnets in accelerators, both of which will be discussed in this paper.

II. MAGNETIC FIELD MODELS

If conductors rather than iron dominate, as is the case for high-field superconducting or bare coil magnets, producing a vertical magnetic field in a vertical slot aperture can be easier than in the horizontal slot required by conventional FFAGs. Fig. 3(a) shows that conductors parallel to the beam direction placed symmetrically above and below a horizontal slot must actually cancel each other at their midpoint in order to produce a pure B_y field on the mid-plane. The field is produced some distance to the side of the coils; normal conducting synchrotron dipoles resemble split solenoids on their side for this reason, with the coil at the periphery of the beam region (and field enhanced by iron).

Reversing the current in one of the conductors so that the fields are additive on the mid-plane produces more field closer to the sources but now the field is horizontal. This problem can be turned into an advantage by rotating the whole magnet so that both the field and aperture slot are vertical: this is the VFFAG situation. It is favourable for conductor-dominated magnets because the field is produced from conductors closer to the beam position and unfavourable for iron-dominated magnets that would make the field perpendicular rather than parallel to the slot sides.

A. Analytic Exponential Model (2D)

For the field in a long magnet with no variation in z, Maxwell's equations in free space reduce to

$$\partial_x B_x + \partial_y B_y = 0, \qquad \partial_x B_y - \partial_y B_x = 0$$

and B_z constant, assumed here to be zero. The solution to these equations that gives the scaling VFFAG field $B_y = B_0 e^{ky}$ and $B_x = 0$ on the mid-plane $x = 0$ is

$$B_y = B_0 e^{ky} \cos kx, \qquad B_x = -B_0 e^{ky} \sin kx.$$

This field is plotted in Fig. 4: its strength increases exponentially with y everywhere, satisfying the scaling law and the field vector rotates with x off the mid-plane.
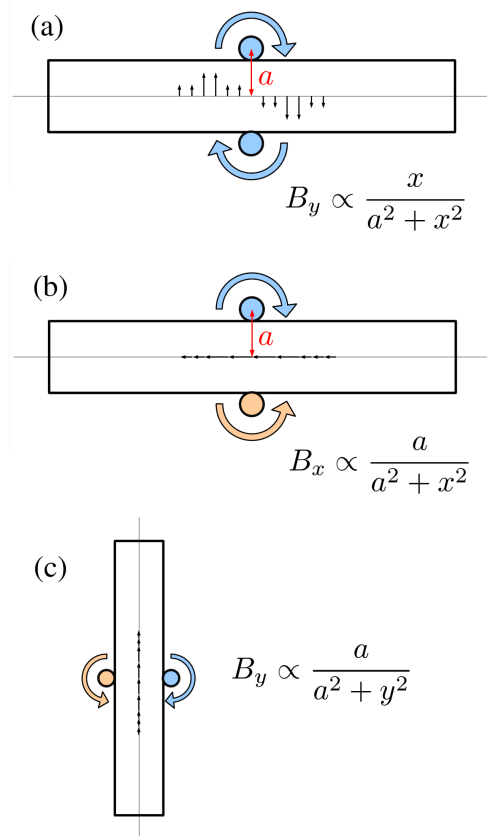

FIG. 3. Pairs of conductors with currents perpendicular to the page that create: (a) a vertical field in a horizontal aperture; (b) a horizontal field in a horizontal aperture; (c) a vertical field in a vertical aperture.
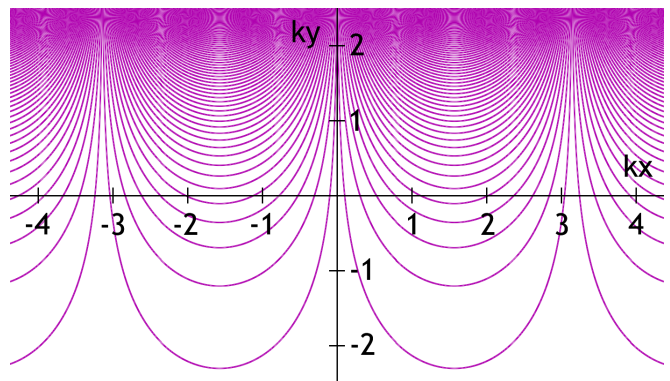

FIG. 4. Transverse field lines of the scaling VFFAG field in a long magnet derived analytically from the complex exponential function.

The 2D free space Maxwell equations are exactly the conditions for the complex function $f(x+iy) = B_y + iB_x$ to be holomorphic. In this case the solution corresponds to $f(z) = B_0 e^{-ikz}$, the complex exponential explaining the appearance of sin and cos in the off-plane field.

B. Block Conductors Model (2D)

To see if the exponential field could be produced by a practical arrangement of superconductors, a 2D model made of rectangular block coils carrying $250\,\mathrm{A/mm^2}$ was optimised to produce the $k = 5\,\mathrm{m^{-1}}$ field from 0.5–4.41 T used in [2]. Fig. 5 shows the result, with the coils on the $+x$ side having opposite polarity to those on the $-x$ side. The exponential field was produced well with small ($< 1\%$) field errors, though in a real magnet the design would be optimised more finely. Because the machine in question had a large energy range of 0.8–12 GeV, the design took advantage of the relativistic beam shrinkage by bringing the coils for the highest energies closer to the mid-plane.
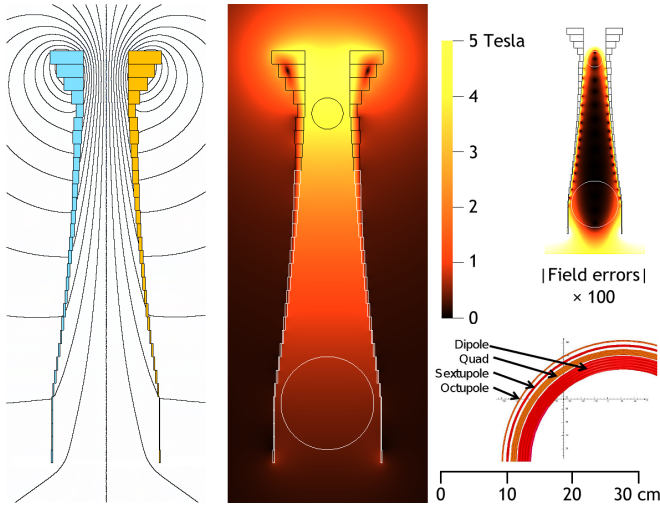

FIG. 5. 2D scaling VFFAG magnet design using block coils. Left: field lines and coils. Centre: field strength and proton beam sizes at 0.8 and 12 GeV. Right: field errors and the size of the superconducting windings in the PAMELA [8] scaling FFAG, to scale.

It is interesting to note that for smaller beams, the magnetised volume could be made very small by narrowing the gap between the conductors into a thin layer. As the conductors have opposite polarity, forces on the coils are away from the mid-plane, so an external support structure in compression should keep them in place.

C. Series Solution with End Fields (3D)

A three-dimensional field model must also include the ends of the magnet. Maxwell's equations for free space will extrapolate the field for the interior of the magnet once it is specified on a plane: here the $x = 0$ mid-plane is chosen. To represent magnets with edge angles, as found in spiral scaling VFFAGs, the parameter $\tau = \tan\theta_{\mathrm{edge}}$ is introduced, along with a coordinate $\zeta = z - \tau y$ so that the magnet corresponds to the region $0 \leq \zeta \leq L_{\mathrm{mag}}$ for all y. Field fall-off is determined by a function $f(\zeta)$

that approaches 1 in the magnet body and 0 outside. Naively one wants a mid-plane field $B_y = B_0 e^{ky} f(\zeta)$ but to obey Maxwell's equation $(\nabla \times \mathbf{B})_x = 0$, this has to be modified to $(B_y, B_z) = B_0 e^{ky}\left(f(\zeta) - \frac{\tau}{k} f'(\zeta), \frac{1}{k} f'(\zeta)\right)$. The note [9] derives this formula and the Taylor series extrapolation used to calculate fields for $x \neq 0$. For edge angles, $z \mapsto z + \tau \Delta y$ is added to the VFFAG scaling law to keep ζ constant (more accurately, this is a rotation of $\tau \Delta y / R$ about the ring centre).
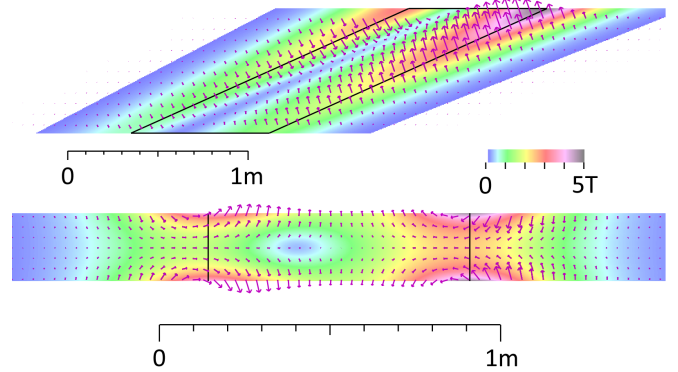

FIG. 6. Cross-section of the 0.8–5 GeV proton driver ring magnet's field in ZY (top) and ZX (bottom) planes. It has $k = 2.01\,\mathrm{m^{-1}}$, $\tau = 2.23$ and $B_0 = 0.5\,\mathrm{T}$.

An example of the resulting field is plotted in Fig. 6. The fringe field at the entrance to the magnet has opposite sign to that at the exit, providing alternating gradient focussing without changing the sign of B_0. Note that symmetry about the YZ plane forbids conventional quadrupole fields, meaning all focussing is skew apart from the B_z component with focussing like a solenoid.

1. Winding Configuration

As with the 2D magnet, the conductors will be parallel to the beam (z axis) in the body of the magnet, running in opposite directions each side of the $x = 0$ mid-plane but the circuits must close somehow at the ends. This should be achieved in practice by the conductors running to the top of the magnet along the $\zeta = 0$ and $\zeta = L$ lines and then looping over to the other side of the mid-plane. In fact, the accumulation of conductors running up the ends of the magnet is what produces the end fields, since Maxwell's equations implicitly require closed circuits with $\nabla \cdot \mathbf{J} = 0$. A detailed 3D model of the winding configuration is a topic for further study.

2. Field Enhancement Factor

As can be seen in Fig. 6, the largest fields are present in the magnet edges and off-plane. The field enhancement

factor

$$F_{\text{enh}} = \frac{\max_z |\mathbf{B}(x,y,z)|}{B_0 e^{ky}} = \frac{B_{\text{fringe}}}{B_{\text{body}}}$$

is plotted in Fig. 7 (at $y = 0$, though by the scaling law it is the same at all y).
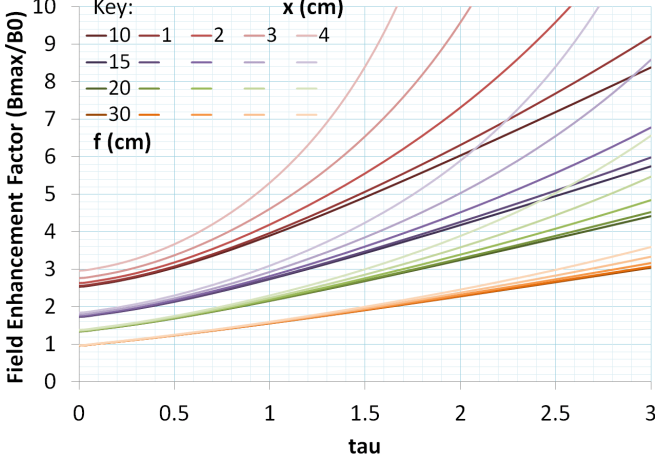

FIG. 7. Field enhancements as a function of τ, fringe length (f) and distance from mid-plane (x) from 0 to 4 cm, in the 3 or 5 GeV magnet design with $k = 2.05\,\text{m}^{-1}$.

Enhancement increases with τ but is ameliorated by increasing fringe length; it also increases extremely rapidly with x for small fringe lengths. However, it decreases with increasing k because higher k magnets actually have weaker fringe fields.

In ring design, this number fills a similar role to the circumference factor of scaling FFAGs: it is the amount a theoretical constant bending field must be multiplied by to find the real maximum field strength in a ring of fixed size and magnet filling factor.

3. Circumference Factor Comparison

Symon [3] defined 'circumference factor' to be the length of the top-energy closed orbit divided by the circumference of a circle with the maximum curvature found anywhere on the orbit, which is equivalent to $C = |\mathbf{B}|_{\text{max}}/\langle B_y \rangle$ where $\langle \cdot \rangle$ denotes average around the orbit. For spiral scaling VFFAGs with a singlet lattice, $C = F_{\text{enh}}/P$ where P is the magnet packing factor. For the proton driver lattices considered in the next section, $F_{\text{enh}} = 2.6$–2.7 and $P^{-1} = 4.3$–5.3, giving $C = 11.2$–14.4 but note that for a synchrotron, $C = P^{-1}$, which will also be much greater than 1. The original MURA note considered FFAGs entirely filled with magnets ($P = 1$) when it quoted values of $C = 5$–6 for scaling FFAGs, so a better metric for comparing realistic rings may be CP. This is just equal to F_{enh} for the spiral VFFAGs and is somewhat lower than the values for sector scaling

FFAGs with reverse bends, even though B_y goes temporarily negative in the spiral VFFAG magnet's exit end field.

III. PROTON DRIVER TRANSVERSE DYNAMICS

Parameters were sought for fixed-field rings to boost the energy of the two ISIS [10] proton bunches from 800 MeV, following the outline RF approach in [11]. Lattice cells containing a single VFFAG magnet and a reasonably-long drift space, with enough dynamic aperture for the 150 mm.mrad geometric emittance proton beam are given in Table I.

TABLE I. Transverse Parameters for VFFAG Rings

$E_{k,\text{inj}}$		800 MeV	
$E_{k,\text{ext}}$	3 GeV	5 GeV	12 GeV
Mean radius		52 m (2×ISIS)	
Superperiods		80 (superperiod is one cell)	
Cell length		4.0841 m	
Drift length		3.3174 m	3.1257 m
Magnet Parameters			
Magnet length		0.7667 m	0.9584 m
B_0		0.5 T	0.4 T
k		2.01 m^{-1}	2.2 m^{-1}
$\tau = \tan\theta_{\text{edge}}$		2.23	2.535
θ_{edge}		65.84°	68.47°
Fringe length		$f = 0.3$ m in $B \propto \frac{1}{2} + \frac{1}{2}\tanh(z/f)$	
B_{ext}	1.3069 T	2.0036 T	3.5274 T
$B_{\text{fringe}}/B_{\text{body}}$		2.6941$_{x=4\,\text{cm}}$	2.6174$_{x=2\,\text{cm}}$
B_{max}	3.5210 T	5.3979 T	9.2326 T
Beam Optics			
$y_{\text{ext}} - y_{\text{inj}}$	0.4780 m	0.6906 m	0.9895 m
μ_u (per cell)		71.17°	71.63°
μ_v		28.60°	19.95°
Q_u (ring)		15.815	15.917
Q_v		6.357	4.433
Matched Injection at Drift Midpoint			
β_u		3.445 m	3.506 m
α_u		0.426	0.481
β_v		7.145 m	10.284 m
α_v		-0.597	-0.960

The beam power will increase in proportion to energy, so options are provided for neutron production at 3 GeV, high-power exotics production at 12 GeV and a 'compromise' energy of 5 GeV, which provides more power for neutrons but perhaps less efficiency. With the mean current 208 μA presently achievable in ISIS, these would have beam powers of 0.6, 2.5 and 1.0 MW respectively at 50 Hz.

The 12 GeV ring, the most aggressive design, with applications to neutrino factories and muon colliders, needed a slightly longer magnet to lower the peak field, which in turn required larger edge angles. The field enhancement was evaluated at $x = 2$ cm and not 4 cm to

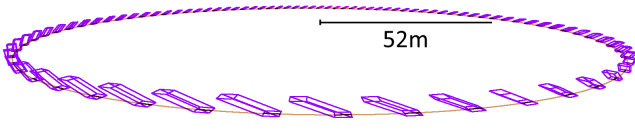account for adiabatic shrinkage of the beam once accelerated to 12 GeV.

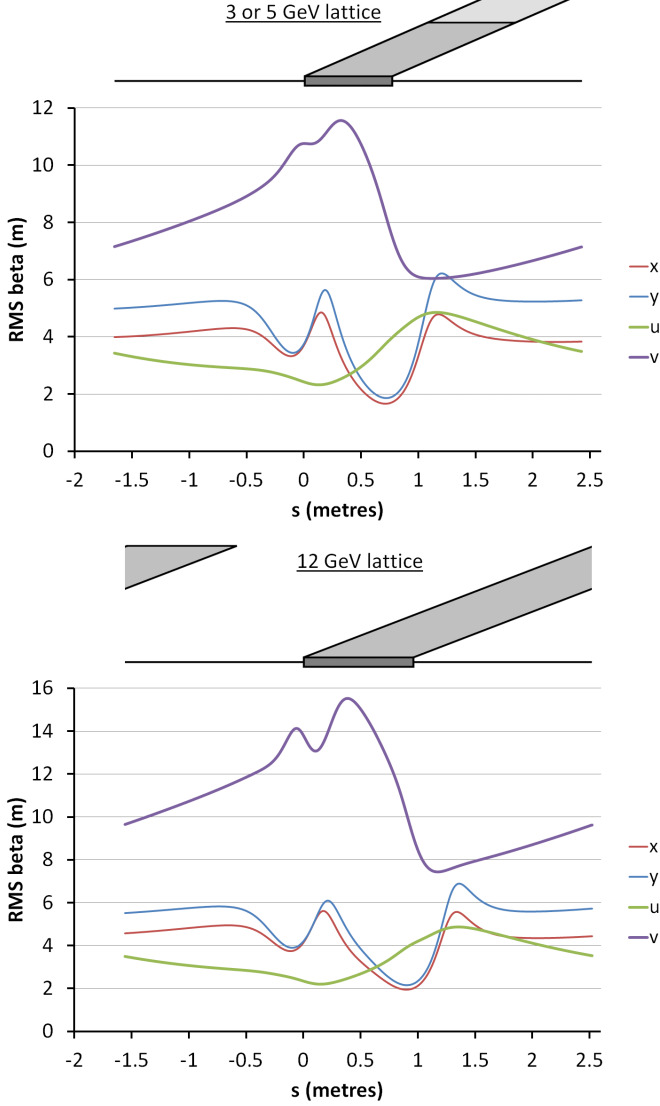FIG. 8. Perspective view of the 12 GeV ring.

FIG. 9. Beta functions in the two lattices, in non-skew and skew coordinates. Magnet size is to scale in z and y.

In terms of skew coordinates u and v, the lattice beta functions shown in Fig. 9 are overall doublet-like but with some features in the end fields. The x and y optics are highly coupled so do not behave like normal beta functions. The cell and machine tunes in Table I are also given in terms of skew axes, although since the weak

focussing in x from the machine curvature couples even these, the values are eigen-tunes that have been labelled as primarily u or v. Fig. 10 shows how the phase spaces vary through the magnet, with some distortion of the matched shape, particularly in the (v, v') plane due to nonlinearity in the magnetic field.
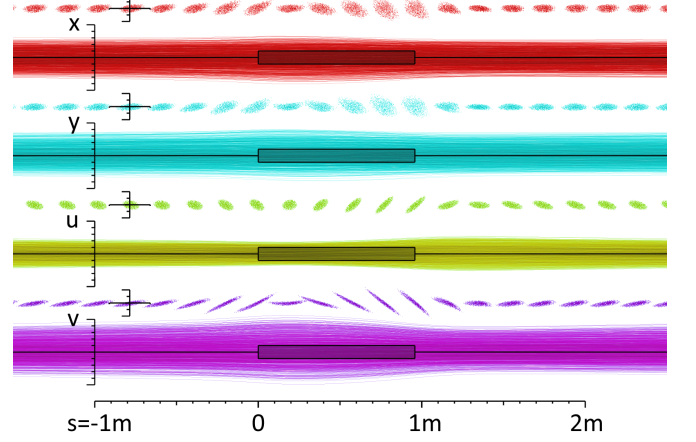

FIG. 10. Phase space and beam evolution through the 12 GeV ring cell at injection energy. Transverse scale is ± 5 cm and x', y', u', v' ranges are ± 20 mrad.

The scaling law gives VFFAGs interesting properties, such as constant dispersions $D_x = 0$ and $D_y = \frac{1}{k}$ and a constant orbit length that makes $\gamma_{tr} = \infty$.
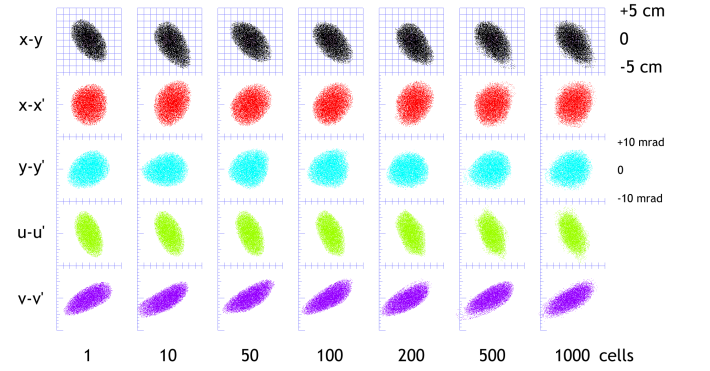

FIG. 11. Tracking through ~ 12 turns of the 12 GeV ring with matched beams (no space charge). Optics stable apart from signs of a 5th order resonance in the (u, u') plane, since $\mu_u \simeq 72°$

A. Dynamic Aperture Parameter Scan

The ring designs were found as combinations of six parameters $(B_0, k, \tau, f, L_{\text{mag}}, L_{\text{drift}})$, the last two being dictated by the integer RF harmonic number (ring circumference) and superperiodicity (cell length) together with B_0, which gives the magnet fill factor. The main focussing parameters k and τ were scanned over, producing

plots like Fig. 12. For each square, 250 protons from a 150 mm.mrad waterbag beam were tracked for 250 cells and removed if $r > 10$ cm. Squares are coloured according to the percentage that survive, showing areas of good dynamic aperture.
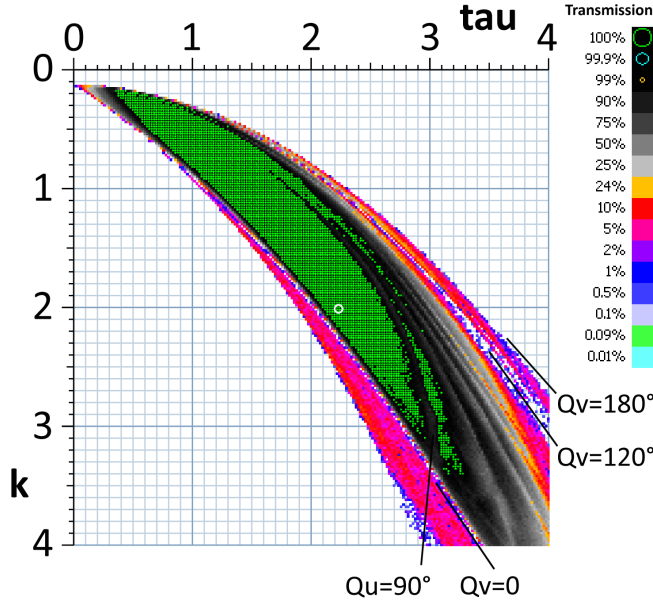

FIG. 12. Proton beam transmission as a function of τ and k, with the 3 or 5 GeV ring design circled. Lines of increased loss correspond to cell tune resonances (labelled).

B. Transverse Intensity Issues

Since the ring tune is 80 times the cell tune, a fine-tuning stage is needed to steer the fractional parts of the ring tunes away from resonances. For the 3 or 5 GeV ring,

$$\frac{\partial Q_{u,v}}{\partial k} = \begin{bmatrix} -8.49 \\ -94.46 \end{bmatrix} \quad \text{and} \quad \frac{\partial Q_{u,v}}{\partial \tau} = \begin{bmatrix} 39.92 \\ 119.82 \end{bmatrix},$$

which are linearly independent enough to find any desired fractional ring tunes without major deterioration of the optics. This fine-tuning will also have to be done on the real machine, using trim coils producing fields proportional to $\partial \mathbf{B}/\partial k$ and $\partial \mathbf{B}/\partial \tau$.

The rapid variation of Q_v arises because the cell tune in v is quite close to zero. This is problematic since Q_v also varies rapidly in response to space charge forces, making the tune depressions of these rings roughly $\Delta Q_{sc,u} = -0.2$ and $\Delta Q_{sc,v} = -0.4$ at injection. This could be improved by finding rings with more balanced tunes or larger mean beta functions, though maybe at the expense of shorter drift spaces or a larger circumference.

IV. PROTON DRIVER LONGITUDINAL DYNAMICS

The line charge density ρ_{1D} along the beam determines the level of transverse as well as longitudinal space charge, so it is important to do realistic simulations of the longitudinal bunch shape including space charge. The simulation code written for this uses three transformations on the particle $(\Delta t, \Delta E)$ coordinates: a drift, an RF kick and a space charge kick; doing these once per turn provides sufficient accuracy. The drift affects Δt depending on the ring circumference function $C(E_k, t)$. For a synchrotron, the absolute time t determines the machine magnet reference momentum p_0, then the particle's E_k gives its $\Delta p/p$, so to first order $C = C_0(1 + \alpha_0 \Delta p/p)$ where α_0 is the momentum compaction (0.0392 for ISIS). Fixed field magnets have no t dependence and for a VFFAG the circumference does not change with closed orbit momentum either, so C is constant. The RF and space charge kicks affect ΔE only, so when done separately from the drift, phase space area is preserved.

RF voltages applied to a proton per turn are defined as $-V_0 \sin(\phi_0 + 2\pi f \Delta t)$, with $V_0(t), \phi_0(t)$ specified by the user. Space charge is calculated using the derivative of the line density, which is Gaussian-smoothed to reduce statistical noise. Provided $\frac{d^2 \rho_{1D}}{dz^2}$ is small, the voltage per turn from space charge is

$$V_{sc} = -C \langle E_{z,sc} \rangle = \frac{C}{4\pi \epsilon_0} \frac{g}{\gamma^2} \frac{d\rho_{1D}}{dz},$$

where g is a shielding factor from the shape of the beam and the conducting beam pipe [12]. ISIS has $g = 1.546$ in a mostly round beam pipe, while the VFFAG has $g = 1.914$ for a skew Gaussian beam between two vertical conducting plates at $x = \pm 4$ cm, calculated using the method in [13].
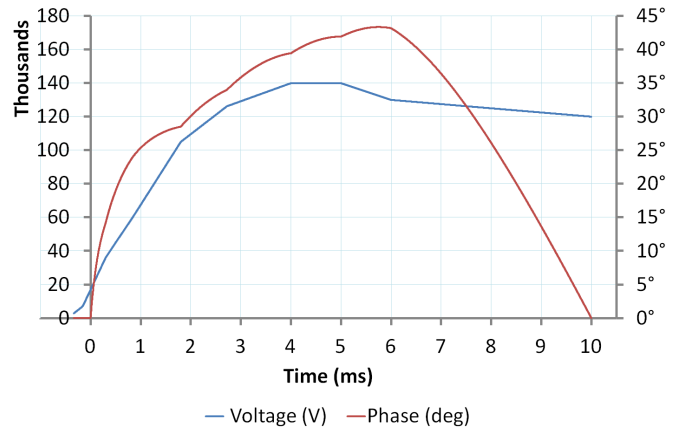

FIG. 13. ISIS first harmonic RF program.

To obtain an input distribution for the VFFAG (and as a check), 1D simulations were first run on ISIS starting from the linac injection at 70.44 MeV. The voltage and phase functions [14] for this are shown in Fig. 13 and

the results in Fig. 14 agree with the current models and observed transmission values of the machine in this mode.
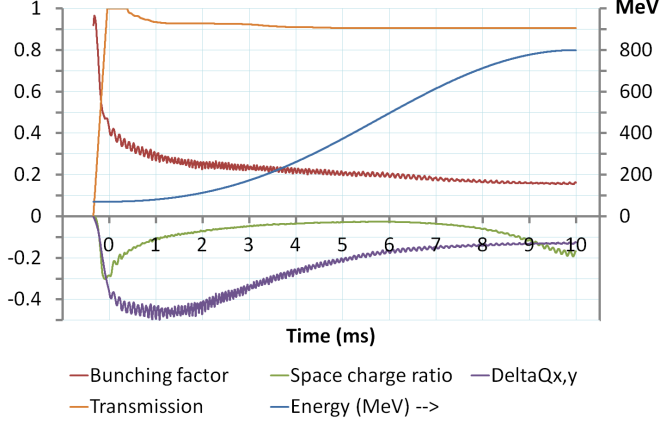

FIG. 14. Bunching factor, transmission and intensity-dependent effects in the ISIS first harmonic simulation.

FIG. 15. RF acceleration program for the 12 GeV VFFAG.

A. Longitudinal Intensity Effects

Fig. 14 shows a number of parameters that could limit machine intensity. The bunching factor is defined as $B = \langle \rho_{1D} \rangle / \rho_{1D}^{\text{peak}}$ with smaller values being worse for space charge. The 'space charge ratio' is defined as an average of $V_{\text{sc}}/V_{\text{rf}}$ over the beam, roughly equivalent to $\Delta Q_s/Q_s$ in terms of the synchrotron tune. It has been shown using the Boussard criterion [15] that this must be greater than -0.4 to avoid microwave instabilities. To avoid dividing by zero when $V_{\text{rf}} = 0$, the ratio is actually calculated as the weighted average $\sum V_{\text{sc}} V_{\text{rf}} / \sum V_{\text{rf}}^2$.

Transverse tune shifts are calculated using the Laslett tune shift formula without boundary terms:

$$\Delta Q_{x,y} = - \frac{q^2}{4\pi\epsilon_0 mc^2} \frac{N}{2\pi B \beta \gamma^2 \epsilon_{x,y}^{\text{n,rms}}} \frac{\bar{\sigma}_{x,y}}{\bar{\sigma}_x + \bar{\sigma}_y},$$

where the last term only requires the average beam aspect ratio $\bar{\sigma}_x/\bar{\sigma}_y$, which is 1 for ISIS and $\bar{\sigma}_u/\bar{\sigma}_v = 0.554$ for the 12 GeV VFFAG. There is a slight inconsistency with the transverse simulations that used a waterbag with $\epsilon_{x,y}^{\text{rms,800MeV}} = 25$ mm.mrad whereas the 1D simulations assumed the value 30 mm.mrad observed in the machine.

B. VFFAG RF System

The VFFAG transfers the two bunches from ISIS into the 1st and 3rd buckets of a frequency-doubled RF system given in Table II. Because of this doubling, the bunch initially fills much of the RF bucket, meaning only low acceleration phases are possible early in the cycle (Fig. 15). Later on, the bunch shrinks in time spread and
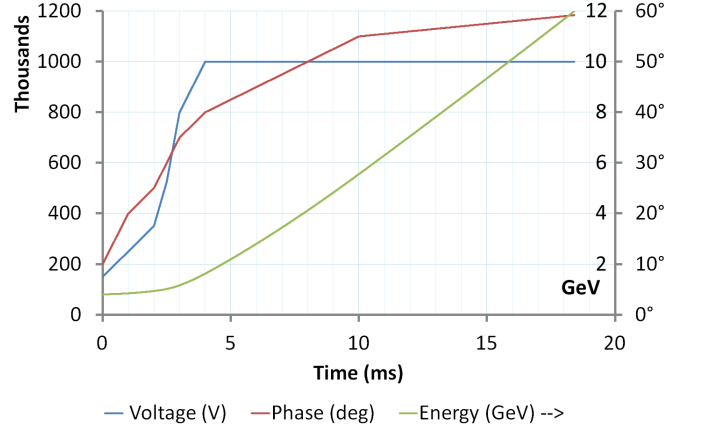
increases in energy spread (Figs. 17,18), allowing faster acceleration.

TABLE II. Longitudinal parameters for the 12 GeV VFFAG. Peak voltage per turn and phase are linearly interpolated from the times given.

RF harmonic	$h = 8$	
RF frequency	6.179–7.321 MHz	
Cycle duration	18.41 ms	
Rep. rate	50 Hz	
Time (ms)	**Voltage (kV)**	**Phase**
0	150	10°
1	250	20°
2	350	25°
2.5	525	30°
3	800	35°
4	1000	40°
10	1000	55°
18.41 (extract)	1000	59.21°
20	1000	60°

In theory the bunch could be adiabatically compressed via an increase in RF voltage early in the cycle, followed by high-phase acceleration. However, as Fig. 16 shows, at low energies of 0.8–1.1 GeV (the first 3 ms) the tune shift in the v plane is high and would exceed the half integer limit if full bunch compression was attempted near injection energy, hence the period of low-phase acceleration.

Table III shows the result of increasing the ISIS linac pulse length by 10 or 20%. Worst-case intensity parameters are shown, which are reasonable for the VFFAG even with 14% more current, although in reality ISIS would use a more efficient RF program or its 2nd harmonic system.
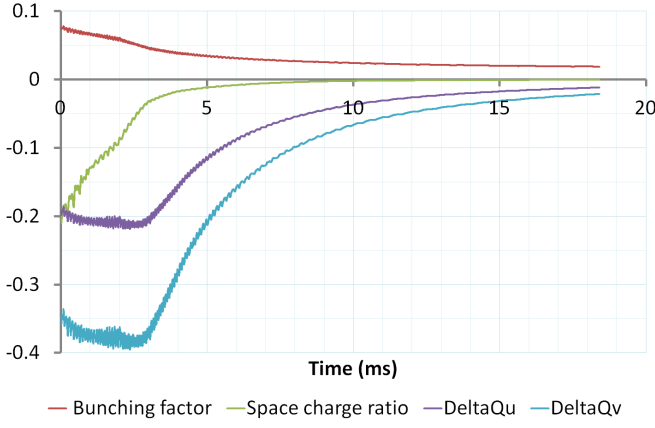
FIG. 16. Bunching factor and intensity-dependent effects in the 12 GeV VFFAG simulation.

TABLE III. Intensity-dependent parameters for the ISIS single harmonic and 12 GeV VFFAG simulations run in series, for different numbers of protons injected into ISIS.

ISIS Protons In	2.50e13	2.75e13	3.00e13
ISIS μA in	200.3	220.3	240.3
ISIS transmission	90.54%	87.95%	85.98%
ISIS protons out	2.26e13	2.42e13	2.58e13
ISIS μA out	181.3	193.7	206.6
ISIS power (kW)	145	155	165
VFFAG transmission		100%	
VFFAG power (MW)	2.18	2.32	2.48
ISIS Peak Intensities			
Bunching factor	0.154	0.150	0.151
Space charge ratio	-0.301	-0.305	-0.311
$\Delta Q_{x,y}$	-0.499	-0.544	-0.580
VFFAG Peak Intensities			
Bunching factor	0.0188	0.0190	0.0190
Space charge ratio	-0.211	-0.257	-0.278
ΔQ_u	-0.219	-0.240	-0.254
ΔQ_v	-0.395	-0.434	-0.458

C. Suitability for Muon Production

Note that in Fig. 17, the output RMS bunch length is small enough to be used for a neutrino factory proton driver [16]. Some of the 1.59 ms spare time for RF reset at the end of the cycle could be used to produce an energy flat top so the two bunches can be extracted with a delay between.

V. FUTURE DEVELOPMENT AND APPLICATIONS

VFFAGs are promising candidates for a number of current accelerator needs, this section explores why and what further work there is to be done.
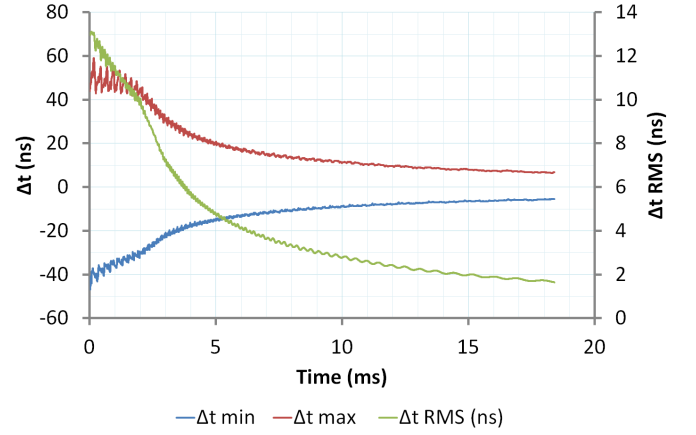

FIG. 17. Bunch duration in the 12 GeV VFFAG simulation, reducing to a final value of $\Delta t_{\rm rms} = 1.64$ ns.
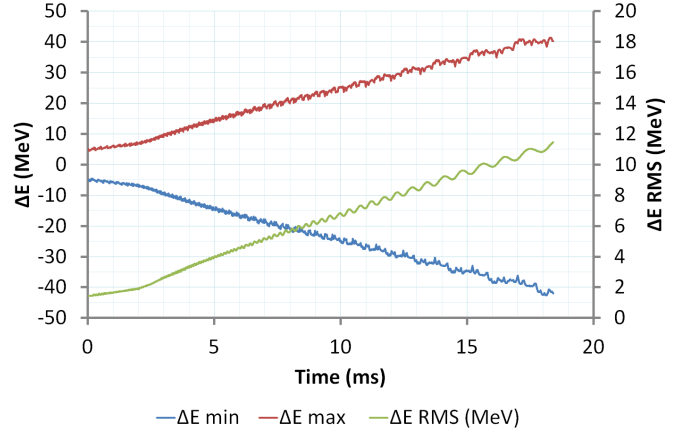

FIG. 18. Increase of bunch energy spread in the 12 GeV VFFAG simulation to ± 41.1 MeV.

A. Improving the Proton Driver Design

The proton driver rings presented in this paper show that in principle a VFFAG can have the right parameters for an ISIS upgrade. However, the lattice needs to be improved to make the machine more practical: although there is enough horizontal drift space for the proposed RF at 25% packing factor [11], the diagonal shape between the magnets is difficult to fit a slotted RF cavity into that spans the whole energy range. The remedy being considered is to make a racetrack-style ring out of two different lattices: an edge-focussed lattice, like the current one but with shorter drifts, designed for maximum bending; and an insertion designed for long drifts but with no bending or edge angles. The insertion could contain RF, collimators, injection and extraction equipment. This design approach has been successfully applied by Mori [17] for scaling FFAGs. Provided the k of the two VFFAG sections is the same, there is no disagreement in closed orbit between them and the matching will be mostly concerned with reducing β ripple.

B. Isochronous VFFAGs for High Average Power

Introducing some horizontal orbit excursion into a VFFAG varies the orbit circumference and allows it to be exactly proportional to beam velocity, making the machine isochronous. This is easier than in a horizontal orbit excursion FFAG (or a cyclotron) because the convergence towards $v/c = 1$ does not cause the orbits to 'pile up' at the maximum radius, producing large gradients and overfocussing. Instead, the vertical orbit motion can control the field gradient and even keep the normalised focussing strength constant.

The orbit excursion follows the path of increasing upward dipole field (where $B_y > 0$ but $B_x = 0$). When this path is at an angle θ to the horizontal in the (x, y) plane, the quadrupole focussing associated with its gradient is at an angle $\theta/2$ to a normal quadrupole. Horizontal FFAGs correspond to $\theta = 0$ and pure VFFAGs to $\theta = 90°$ with the quadrupole then rotated by $\theta/2 = 45°$. For an isochronous VFFAG that is not ultra-relativistic, these angles will vary as the beam accelerates, tending towards $\theta = 90°$ as $v \to c$.

Isochronous machines may use a fixed frequency RF system, which generally has a higher gradient than variable-frequency RF. If the orbit turns are also separated at injection and extraction, the VFFAG can operate in CW mode like a cyclotron. Isochronous VFFAGs could potentially have the same beam current as a cyclotron but a much higher (relativistic) extraction energy, yielding an average beam power of many megawatts. Such machines may be of interest for nuclear waste transmutation.

1. Complete Isochronism in Strong Focussing Rings

For rings dominated by strong focussing (i.e. large rings very unlike a cyclotron), it is possible to find an orbit excursion that is isochronous and fixed tune analytically. As the VFFAG is also fixed-field, this satisfies all of Teichmann's 'complete isochronism' conditions [7].

For isochronism, the mean orbit radius must be $r = \beta R$ for some R and for the orbit to close, $\langle B_y \rangle = p/qr = m\beta\gamma c/(q\beta R) = \gamma B_0$ where $B_0 = mc/qR$. This is familiar as the field relation for an isochronous cyclotron. Assume B_y varies in sectors around the machine but always retains the scaling with γ. The normalised focussing of a magnet is $B'l/p$ where $l = r\Theta$ is the sector magnet length at momentum p and B' is the magnitude of the quadrupole gradient, regardless of quadrupole orientation.

$$\frac{B'l}{p} = \frac{B'r\Theta}{m\beta\gamma c} = \frac{B'\beta R\Theta}{m\beta\gamma c} = \frac{B'}{\gamma}\frac{R\Theta}{mc} \propto \frac{B'}{\gamma},$$

so B' must be proportional to γ to keep normalised focussing (and hence machine tunes) constant. However, this means $\mathrm{d}B_y/\mathrm{d}s \propto \gamma \propto B_y$, where s is path length in (x, y) along the orbit excursion curve. Thus $B_y = B_0 e^{s/S}$

for an appropriate choice of origin for s and $S = 1/k$ is the *scaling length*. In other words, the dipole field must increase exponentially along the orbit excursion curve to retain scaling optics.

The actual shape of the orbit excursion is found via the relation between β and γ:

$$r = \beta R = r\sqrt{1 - \gamma^{-2}} = R\sqrt{1 - e^{-2s/S}}$$

relates arc length to r. It also provides a lower bound to the energy used in such a machine because after some manipulation,

$$\frac{\mathrm{d}r}{\mathrm{d}s} = \frac{R}{S}\frac{1}{\beta\gamma^2}$$

but $\mathrm{d}r/\mathrm{d}s \leq 1$ because s is path length, therefore

$$\beta\gamma^2 \geq \frac{R}{S}$$

in a strong-focussing-dominated, isochronous VFFAG with scaling optics. The equality $\beta\gamma^2 = R/S$ occurs at the minimum energy when the orbit excursion is horizontal. S dictates the separation of the orbits, so reducing S allows the acceleration to start from lower energies but increases the size of the magnets in the machine.

It should be noted that in smaller machines, the weak focussing in x from the rotation around the ring is significant and in fact dominant in many cyclotrons. Cyclotrons clearly work to much lower energies, so an analysis including weak focussing may keep the eigen-tunes constant to lower energies if the ring tunes are low.

2. Electron VFFAGs and eRHIC

The lower bound on energy for a scaling isochronous VFFAG gets easier to satsify the lower the mass of the particle being accelerated. For electron machines in the GeV scale, the difference from the speed of light becomes negligible and a scaling VFFAG with a purely vertical orbit excursion can be used.

Some recent ongoing work [18] has investigated the use of such a VFFAG for the proposed eRHIC project where an electron beam is recirculated through a fixed-frequency linac several times in the RHIC tunnel and then decelerated in the same machine, out of phase, for energy recovery. The energy range in one example was 1.2–10 GeV over 8 linac passes. $k = 100\,\mathrm{m}^{-1}$ was used, meaning the turns fitted within an orbit excursion of 21.2 mm. Here a single VFFAG transfer line replaced either a cascade of two non-scaling FFAGs, or several stacked ring transfer lines, due to its acceptance of a high momentum range with stable optics in a small aperture.

C. Hadron Therapy

Finally, VFFAGs may be of interest for medical proton and ion therapy machines. The PAMELA [19] study has

investigated conventional FFAGs for these applications because of their advantages of compactness and rapid cycling over synchrotrons. Compactness comes from their use of superconducting bending magnets and allows the machine to fit more easily in a hospital, while rapid cycling comes from not having to ramp the magnets and allows radiation doses to be applied with a finer resolution within the patient.

Since the beam in these applications is transversely small, the VFFAG style magnet (see section II B) may reduce the magnet volume down to a narrow slot, further reducing the amount of material and power used in the machine, while still preserving the other advantages of FFAGs listed above.

[1] *Mark V FFAG. Equations of Motion for Illiac Computation*, J.L. Powell, equation (1) in MURA report 80, available from `http://cdsweb.cern.ch/record/1052338/files/cer-002709483.pdf` (1955).

[2] S.J. Brooks, *Vertical Orbit Excursion FFAGs*, in *Proc. HB2010*.

[3] K.R. Symon, *The FFAG Synchrotron—Mark I*, MURA note 043 (1954).

[4] D.J. Kelliher (RAL), private communication.

[5] T. Ohkawa, *FFAG Electron Cyclotron* abstract, Physical Review **100** p.1247 (1955).

[6] G. Leleux, J. Proy and M. Salvat, *FFAG Helicoïdal: Etude de la Stabilite Betatron*, Rapport OC 70, Service de Physique Appliquee Section d'Optique Corpusculaire (1959).

[7] J. Teichmann, *Accelerators with Vertically Increasing Field*, translated from Atomnaya Énergiya, Vol.12, No.6, pp.475–482 (1962).

[8] Holger Witte *et al.*, *PAMELA Magnets—Design and Performance*, in *Proc. PAC 2009*.

[9] S.J. Brooks, *Fringe Fields for VFFAG Magnets with Edge Angles*, available from `http://stephenbrooks.org/ral/report/2011-6/skewVFFAGfringes.pdf` (2011).

[10] B. Boardman, ed., *Spallation Neutron Source: Description of Accelerator and Target*, Rutherford Appleton Laboratory technical report RL-82-006 (1982).

[11] S.J. Brooks, *Extending the Energy Range of 50 Hz Proton FFAGs*, section 'Design Parameters', in *Proc. PAC 2009*.

[12] R. Baartman, *Form Factor g In Longitudinal Space Charge Impedance*, TRIUMF design note 1992-TRI-DN-K206, available from `http://lin12.triumf.ca/text/design_notes/k206/k206h.pdf`.

[13] S.J. Brooks, *Arbitrary Beams in Uniform Pipes*, section 2.6.2 'Elliptical Gaussian Beam', available from `http://stephenbrooks.org/ral/report/2012-6/abeamupipe.pdf` (2012).

[14] C.R. Prior (RAL), private communication.

[15] A. Hofmann and F. Pedersen, *Bunches with Local Elliptic Energy Distribution*, section 'Microwave instabilities', in *Proc. PAC'79*.

[16] The IDS-NF collaboration, *Interim Design Report*, Table V 'Proton driver requirements', p.55, RAL-TR-2011-018.

[17] JB. Lagrange, Y. Mori *et al.*, *Applications of Advanced Scaling FFAG Accelerator*, in *Proc. IPAC 2010*.

[18] D. Trbojevic (BNL), private communication.

[19] *PAMELA Overview: Design Goals and Principles*, K. Peach *et al.*, Proc. PAC 2009.